International Forum on Aeroelasticity and Structural Dynamics
IFASD 2026
16-18 June 2026, Goettingen, Germany

ON THE FLUTTER MECHANISM DRIVEN BY SECOND BENDING-FIRST TORSION COUPLING IN HIGH-ASPECT RATIO WINGS

M. Pirnay[1], E. Verstraelen[1], S. Dosse[2], X. Amandolese[2], T. Andrianne[1]

[1]Department of Aerospace and Mechanical Engineering, University of Liège
Allée de la Découverte 9, Liège, Belgium
maxime.pirnay@uliege.be
everstraelen@uliege.be
t.andrianne@uliege.be

[2]LMSSC, Conservatoire National des Arts et Métiers
Paris, France
simon.dosse@lecnam.net
xavier.amandolese@lecnam.net

Keywords: IFASD, aeroelasticity, coupled-mode flutter, hump mode

Abstract: The present work investigates the flutter mechanism driven by second bending (B2) - first torsion (T1) modal coupling in high-aspect-ratio wings through wind tunnel experiments and a reduced-order aeroelastic model. Two taut-strip wings sharing the same airfoil profile but differing in structural properties are tested in two low-speed wind tunnels. Despite their geometrical similarity, the two wings exhibit significantly different aeroelastic behaviours: one undergoes flutter while the other remains stable, both displaying a hump-shaped damping variation characteristic of B2-T1 coupling. A Rayleigh-Ritz structural formulation coupled with Theodorsen's unsteady aerodynamics is validated against experimental frequency and damping trends. The spanwise distribution of aerodynamic work density shows that the vibration node of the second bending mode separates regions of energy input and dissipation, and that a strong dissipative contribution near the wing tip promotes the hump-mode restabilisation. Examination of the modal content indicates that a greater participation of the first bending mode enhances the bending-torsion energy exchange, thereby favouring flutter onset.

1 INTRODUCTION

In recent decades, advances in aerospace engineering have intensified research effort in aeroelasticity. The continuous demand for improved aerodynamic efficiency, reduced fuel consumption, and lower structural mass has led to the development of increasingly flexible wings with high aspect ratios. While these design trends offer significant aerodynamic benefits, they also introduce new fluid–structure interaction challenges due to the increased flexibility of wings [1–3].

Among these instabilities, classical flutter (or coupled-mode flutter) has been the most thoroughly studied due to its critical implications for flight safety and performance. Its mechanism is well understood from two-degree-of-freedom typical airfoil section model up to high-complexity wings and is widely covered in fundamental aeroelastic textbooks [4, 5]. However, high-aspect-ratio wings introduce additional complexity through their closely spaced low-frequency bending modes [3, 6]. When the first two bending modes have natural frequencies

lower than that of the first torsional mode, a different type of flutter mechanism involving second bending-first torsion (B2-T1) can occur. This flutter scenario is of particular interest, as it differs from the classical coupled-mode flutter.

Loring's wing [7] constitutes the earliest documented experimental benchmark of a high-aspect-ratio, straight uniform cantilever wing whose flutter mechanism is governed by the second bending-first torsion modal coupling. This specific instability scenario has since motivated a large amount of experimental and numerical investigations on increasingly flexible configurations. Among the most referenced cases are the high-aspect-ratio wing of Tang and Dowell [8], the highly flexible Pazy wing [9], specifically designed as a geometrically nonlinear aeroelastic benchmark at large deflections, and the taut-strip flexible wing developed at ONERA [10], conceived to reproduce this flutter mechanism in low-to-moderate Reynolds numbers.

The B2-T1 instability is associated with a specific dynamic signature known as the hump mode. Unlike classical flutter, where modal damping decreases monotonically with airspeed until it crosses zero, the hump mode is characterized by a non-monotonic variation of modal damping as shown in Figure 1: damping first decreases, then recovers at higher airspeed. Depending on the structural and aerodynamic parameters, this minimum damping may or may not cross the neutral stability boundary [11]. The hump mode can lead to an instability region which, in highly flexible configuration such as Pazy wing, is found to shift toward lower airspeed as static wing deflection increases under aerodynamic loads. This effect requires geometrically nonlinear aeroelastic frameworks to be properly captured [9, 12].

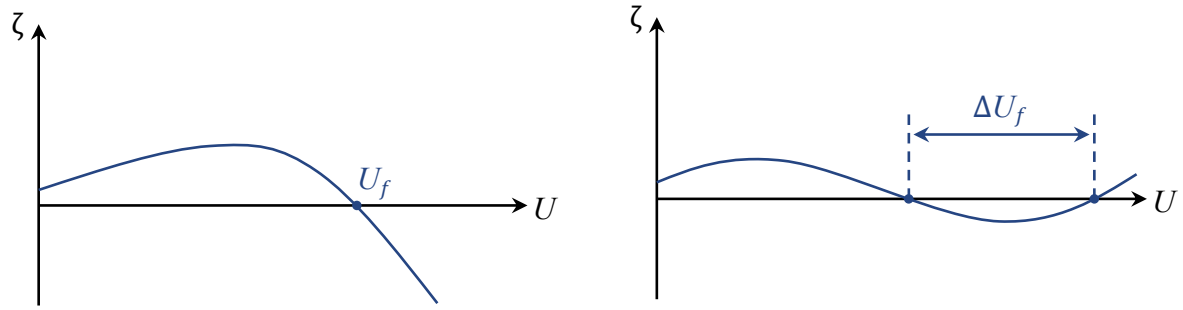

Figure 1: Schematic representation of damping variation for classical flutter mode (left) and hump mode (right). Reproduced from [11].

The present study is based on a reduced-order aeroelastic model, coupling a Rayleigh–Ritz structural formulation with Theodorsen's unsteady aerodynamics [13]. Two dedicated wind tunnel experiments following a taut-strip architecture [10] operating at low airspeeds are investigated. The static aeroelastic deformations are limited to small amplitudes such that this deformation-dependent shift remains negligible and a linearised modelling framework is sufficient. Two wing configurations are investigated: one tested at the Institut AéroTechnique (IAT/Cnam) wind tunnel [14] and one at the ULiège wind tunnel [15]. Both wings are designed to exhibit B2-T1 flutter within their respective operational envelopes. An energy-based analysis combined with an examination of the modal content of the flutter mode is proposed to identify the physical mechanisms governing the instability.

2 EXPERIMENTAL SETUPS

The first wing, Wing 1, is rigidly mounted in the S4 low-speed wind tunnel of IAT/Cnam. It consists of 12 NACA0015 sections assembled on an H-shaped aluminium spar, with a half-span

$s = 1.5$ m and a chord $c = 0.2$ m. The elastic axis (EA) is located at $c/3$ and the center of gravity (CG) at $0.379c$. A wingtip device is attached, with mass $M_{\mathrm{t}} = 0.362$ kg, rotational inertia $I_{\mathrm{t,y}} = 10^{-3}$ kg m^2, and a chordwise offset $X_{\mathrm{t}} = 0.007$ m from the elastic axis. Wing 1 is equipped with DuraAct P-876.A15 and MFC M8528-F1 piezoelectric patches, which can serve as control actuators but are used in the present study solely as structural exciters. The second wing, Wing 2, is mounted in the multidisciplinary wind tunnel of ULiège. It shares the same number of sections, mounted on a rectangular aluminium spar, with $s = 1.2$ m, $c = 0.16$ m, an elastic axis at $c/4$, and a center of gravity at $0.442c$. No wingtip device was fitted, as a wider airspeed range was achievable in that facility. Pictures of both setups are shown in Figure 2. The inset in the left picture shows the wingtip device installed on Wing 1.

Both wings are instrumented with accelerometers and laser displacement sensors. On Wing 1, two miniature piezoelectric ICP accelerometers (PCB Piezotronics model M352C65, sensitivity 100 mV/g, range ± 50 g) are located inside the wingtip, and two pairs of optoNCDT 1420 laser sensors measure displacements at mid-span and tip sections. In addition, an ATI six-axis force/moment sensor measures the unsteady loads. On Wing 2, a single wireless MEMS DC accelerometer and a SICK OD2-P300W200I0 laser displacement sensor are located at the tip trailing edge. Dynamic pressure is obtained from a Pitot tube in each test section.

The modal parameters are extracted from the time responses using the covariance-driven stochastic subspace identification (SSI-cov) method [16]. The frequencies and damping ratios are identified from output signals without requiring knowledge of the input excitation, modelled instead as a stochastic process. The model order is prescribed and stabilization diagrams are used to separate physical from spurious modes by applying tolerance criteria on frequency and damping ratio between successive model orders [17] (see Appendix B). Identification uncertainty is quantified via block bootstrap resampling, repeating SSI-cov on each surrogate to derive standard deviation estimates for each mode [18].

Figure 2: Experimental wind tunnel set-ups for the two wings: Wing 1 (left) and Wing 2 (right).

3 LINEAR AEROELASTIC MODEL

The aeroelastic model considers two degrees of freedom: out-of-plane bending $h(y,t)$ and torsion $\alpha(y,t)$. The chordwise displacement is assumed negligible. A wingtip device is incorporated through a Dirac function $\delta = \delta(y-s)$ acting at the wing tip. The linearised equations of motion read

$$\begin{aligned} (m + M_{\mathrm{t}}\delta)\,\ddot{h} + c_h\,\dot{h} + \Big(EI_x\,h''\Big)'' + S_\alpha\,\ddot{\alpha} &= -L, \\ (I_\alpha + I_{\mathrm{t},y}\,\delta)\,\ddot{\alpha} + c_\alpha\,\dot{\alpha} - \Big(GJ\,\alpha'\Big)' + S_\alpha\,\ddot{h} &= M_{EA}, \end{aligned} \tag{1}$$

where $S_\alpha = (m + M_{\mathrm{t}}\delta)\,X_\alpha$ denotes the static unbalance about the elastic axis introducing X_α the offset between CG and EA (*i.e.* $X_\alpha = X_{CG} - X_{EA}$). The deformation is approximated using a Rayleigh-Ritz decomposition [4, 8]

$$h(y,t) = \sum_{i=1}^{N_h} \phi_{h,i}(y)\,q_{h,i}(t), \qquad \alpha(y,t) = \sum_{j=1}^{N_\alpha} \phi_{\alpha,j}(y)\,q_{\alpha,j}(t), \tag{2}$$

where the assumed mode shapes ϕ are those of a cantilever beam with a lumped tip mass [19]. Projecting the equations of motion onto the retained modes yields

$$\mathbf{M}\,\ddot{q} + \mathbf{C}\,\dot{q} + \mathbf{K}\,q = F_a, \tag{3}$$

with $q = [q_{h,1} \dots q_{h,N_h}\ q_{\alpha,1} \dots q_{\alpha,N_\alpha}]^T$. The aerodynamic forcing F_a is modelled using Theodorsen's unsteady aerodynamic theory [13]. Following the notation of Wright and Cooper [20], the motion-induced lift and moment are expressed as

$$\begin{aligned} L &= \rho U^2\Big(L_h\,h + \tfrac{b}{U}\,L_{\dot{h}}\,\dot{h} + \tfrac{b^2}{U^2}\,L_{\ddot{h}}\,\ddot{h}\Big) + \rho b U^2\Big(L_\alpha\,\alpha + \tfrac{b}{U}\,L_{\dot{\alpha}}\,\dot{\alpha} + \tfrac{b^2}{U^2}\,L_{\ddot{\alpha}}\,\ddot{\alpha}\Big), \\ M_{EA} &= \rho b U^2\Big(M_h\,h + \tfrac{b}{U}\,M_{\dot{h}}\,\dot{h} + \tfrac{b^2}{U^2}\,M_{\ddot{h}}\,\ddot{h}\Big) + \rho b^2 U^2\Big(M_\alpha\,\alpha + \tfrac{b}{U}\,M_{\dot{\alpha}}\,\dot{\alpha} + \tfrac{b^2}{U^2}\,M_{\ddot{\alpha}}\,\ddot{\alpha}\Big), \end{aligned} \tag{4}$$

where $L_h, L_{\dot{h}}, \dots$ and $M_h, M_{\dot{h}}, \dots$ are the oscillatory aerodynamic derivatives. Casting the system in state-space form with $x = [\dot{q}\ \ q]^T$ gives

$$\dot{x} = \mathbf{A}\,x, \qquad \mathbf{A} = \begin{bmatrix} -\mathbf{M}^{-1}\mathbf{C} & -\mathbf{M}^{-1}\mathbf{K} \\ \mathbf{I} & \mathbf{0} \end{bmatrix}, \tag{5}$$

where $\mathbf{M} = \mathbf{M}_S + \mathbf{M}_A$, $\mathbf{C} = \mathbf{C}_S + \mathbf{C}_A$, and $\mathbf{K} = \mathbf{K}_S + \mathbf{K}_A$ are the combined structural and aerodynamic mass, damping, and stiffness matrices. All matrix expressions are given in Appendix A, and the complete model development is detailed in [15].

4 EXPERIMENTAL RESULTS

4.1 Wind-off analysis

A white noise signal is supplied to Wing 1 via the piezoelectric patches using a USB-6363 DAQ unit. For Wing 2, modal parameters are extracted from impulse responses. Both excitation strategies yield sufficient frequency content to identify all the modes of interest.

The inertial properties are either directly measured or derived from CAD data. The stiffness terms are obtained from the wind-off modal results, and damping ratios are identified via SSI-cov. The resulting wind-off characteristics of both wings are summarized in Table 1. In both cases, the second bending frequency is lower than the first torsional frequency.

Table 1: Wind-off characteristics of the wings.

Characteristics	Wing 1	Wing 2	Unit
Wing properties			
Semi span, s	1.5	1.2	m
Chord, c	0.2	0.16	m
Half-chord, b	0.1	0.08	m
CG location from LE, X_{CG}	$0.379c$	$0.442c$	m
EA location from LE, X_{EA}	$c/3$	$c/4$	m
Mass per unit length, m	2.55	1.105	kg/m
Moment of inertia per unit length, I_α	5.55×10^{-3}	3.06×10^{-3}	kg m^2/m
Flapwise bending stiffness, EI_x	363.8	21.17	N m^2
Torsional stiffness, GJ	80.4	24.2	N m^2
Wingtip properties			
Tip mass, M_t	0.362	-	kg
Tip moment of inertia, $I_{\mathrm{t,y}}$	1×10^{-3}	-	kg m^2
Tip CG offset from EA, X_t	7×10^{-3}	-	m
Modal properties			
1$^{\mathrm{st}}$ bending frequency of the coupled system, f_1	2.53	1.69	Hz
2$^{\mathrm{nd}}$ bending frequency of the coupled system, f_2	16.31	10.54	Hz
1$^{\mathrm{st}}$ torsion frequency of the coupled system, f_3	18.36	23.24	Hz
1$^{\mathrm{st}}$ bending modal damping ratio, ζ_1	1.9	1.6	%
2$^{\mathrm{nd}}$ bending modal damping ratio, ζ_2	0.2	0.8	%
1$^{\mathrm{st}}$ torsion modal damping ratio, ζ_3	0.4	0.6	%

4.2 Wind-on static analysis

The motion-induced unsteady aerodynamic loading, according to Theodorsen lift and moment formulations, depends on the steady lift and pitching moment slopes with the angle of attack. A first set of experiments is carried out to measure the steady aerodynamic coefficients of Wing 1 at $Re \simeq 2.7 \times 10^5$ and angle of attack ranging from -5 to $5°$, *i.e.* in attached flow conditions. For each angle of attack, the coefficients were obtained by averaging 16 s of the force sensor signals acquired at a sampling frequency of 1024 Hz. The wing torsional deformation is monitored and remains lower than $0.4°$ at the tip.

The variation of lift and moment coefficients about the elastic axis with the root angle of attack α_r are reported in Figure 3. Three configurations of Wing 1 are considered: with wingtip, without wingtip, and without wingtip with sealed gaps. Each tested configuration exhibits a quasi-linear variation of the lift and moment coefficient with the wing root angle of attack. The wingtip has no significant effect on the aerodynamic coefficients. In contrast, the small gaps (3mm, *i.e.* 0.2% of the span) significantly impact the aerodynamic slopes.

For the unsealed configurations, the measured lift and moment slopes are $\mathrm{d}C_L/\mathrm{d}\alpha_r \simeq 4.25$ and $\mathrm{d}C_{M_{\mathrm{EA}}}/\mathrm{d}\alpha_r \simeq 0.52$, respectively, whereas sealing the gaps increases these values to $\mathrm{d}C_L/\mathrm{d}\alpha_r \simeq 4.84$ and $\mathrm{d}C_{M_{\mathrm{EA}}}/\mathrm{d}\alpha_r \simeq 0.59$.

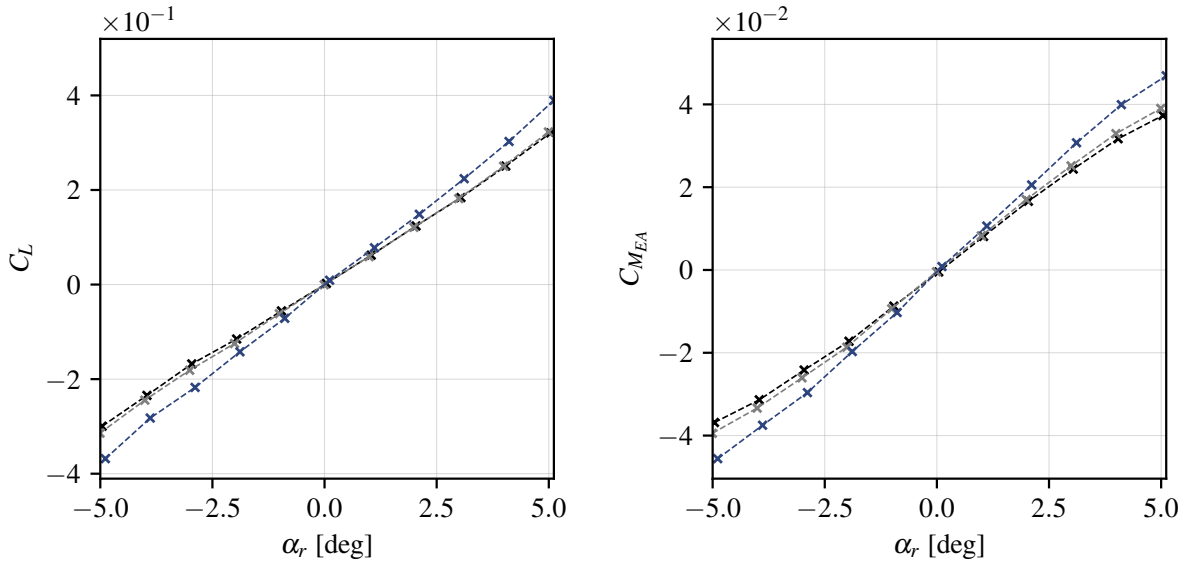

Figure 3: Lift (left) and moment (right) coefficient about the elastic axis versus angle of attack at $Re \simeq 2.7 \times 10^5$ for Wing 1: without wingtip (black), with wingtip (grey), and without wingtip with sealed gap (blue).

4.3 Wind-on dynamic analysis

Aeroelastic tests are performed for both wings in the unsealed configuration, so that the lift and moment slopes $\mathrm{d}C_L/\mathrm{d}\alpha_r \simeq 4.25$ and $\mathrm{d}C_{M_{\mathrm{EA}}}/\mathrm{d}\alpha_r \simeq 0.52$ are used to weight the circulatory terms of the Theodorsen lift and pitching moment formulations. Since both wings share the same NACA0015 profile and gap configuration, these aerodynamic coefficients are applied consistently across configurations.

Owing to the significant differences in the wind-off natural frequencies of the two wings (see Table 1), frequencies are non-dimensionalized using the uncoupled torsional frequency f_α [19], which also serves as the reference frequency in the reduced velocity $U^* = U/(2\pi f_\alpha b)$. At each reduced velocity, the modal parameters extracted from the time responses using SSI-cov are compared against the model predictions in Figure 4. The uncertainty obtained via block bootstrap resampling is also indicated. The uncertainty in frequency remains negligibly small, while non-negligible uncertainty is only visible in the damping of the stabilized mode at high velocity. Wing 1 exhibits no flutter within the tested range, which was limited by the wind tunnel maximum airspeed. The flutter mode damping reaches a minimum of $\zeta = 9.3 \times 10^{-4}$ at the highest tested airspeed. The aeroelastic model predicts damping recovery at higher airspeeds, consistent with a stable hump-mode scenario. For Wing 2, the model predicts flutter arising from B2–T1 coupling at $U^* = 5.1$. Experimentally, Wing 2 undergoes flutter at $U^* \simeq 5$, leading to failure at the wing's mounting point.

Both wings share the same airfoil profile, taut-strip architecture, and aerodynamic coefficients, and differ only in their structural properties. In both cases, the instability arises from the coupling of B2 and T1 modes, leading to a hump-type damping variation. Despite these similarities, the model predicts markedly different aeroelastic behaviours: Wing 1 remains stable across the entire airspeed range while Wing 2 exhibits a clear flutter region. The flutter mechanism is investigated in section 5 through an energy-based analysis and an examination of the modal content of the flutter mode.

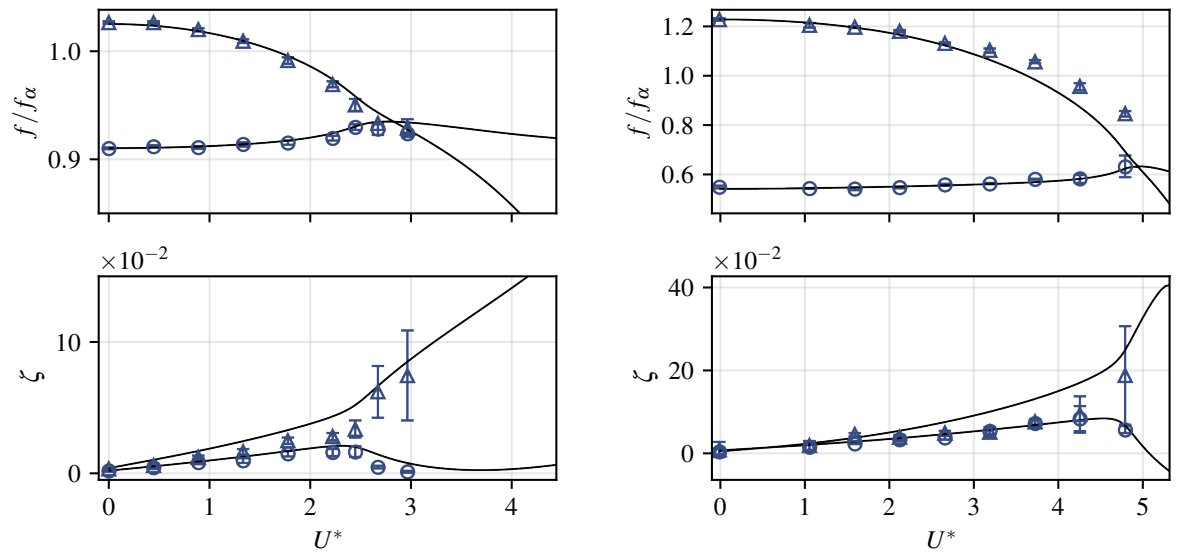

(a) Wing 1.

(b) Wing 2.

Figure 4: Experimental and numerical frequency and damping variation with airspeed. Experimental data are indicated by blue circle (B2) and blue triangle (T1), while the solid black line denotes the model prediction.

5 FLUTTER MECHANISM

The flutter mechanism is investigated through the total work W_{aero} of the aerodynamic forces over a cycle of prescribed harmonic motion, computed from the velocity-dependent eigenvectors. Neglecting structural damping, negative values of this work ($W_{\text{aero}} < 0$) indicate a stabilising energy transfer from the structure to the flow, while positive values ($W_{\text{aero}} > 0$) correspond to a destabilising transfer from the flow to the structure. Since the B2 mode shape exhibits a vibration node along the span, alternating regions of stabilising and destabilising aerodynamic work are expected. The total aerodynamic work W^j_{aero} associated with the jth aeroelastic mode, over one oscillation period $T_j = 1/f_j$, is constructed from its spanwise distribution $w^j_{\text{aero}}(y)$ as

$$W^j_{\text{aero}} = \int_0^s w^j_{\text{aero}}(y)\,\mathrm{d}y = \int_0^s \int_0^{T_j} \left[-L^j(y,t)\dot{h}^j(y,t) + M^j_{EA}(y,t)\dot{\alpha}^j(y,t)\right] \mathrm{d}t\,\mathrm{d}y, \tag{6}$$

The kinematics of the motion are reconstructed from the complex eigenvectors of the state matrix $\mathbf{A}$ at a given airspeed. For the j^{th} mode, it reads

$$\begin{aligned} h^j(y,t) &= \mathfrak{Re}\left(e^{2i\pi f_j t}\left[\sum_{i=1}^{N_h} \phi_{h,i}(y)\frac{v^j_{h,i}}{v^j_{\alpha,1}}\alpha_0\right]\right), \\ \alpha^j(y,t) &= \mathfrak{Re}\left(e^{2i\pi f_j t}\left[\sum_{n=1}^{N_\alpha} \phi_{\alpha,n}(y)\frac{v^j_{\alpha,n}}{v^j_{\alpha,1}}\alpha_0\right]\right), \end{aligned} \tag{7}$$

where the bending and torsional modal coordinates $v^j_{h,i}$ and $v^j_{\alpha,n}$ are extracted from the j^{th} aeroelastic eigenvector and normalized with respect to the first torsional coordinate $v^j_{\alpha,1}$. Assuming harmonic motion, the complex eigenvector components directly provide the amplitude and phase of each degree of freedom. The modal displacements are reconstructed by superimposing the assumed mode shapes $\phi_{h,i}(y)$ and $\phi_{\alpha,n}(y)$, weighted by their respective modal

coordinates, and a torsional amplitude $\alpha_0 = 3°$ is prescribed at the first torsional coordinate to scale the motion. The resulting aerodynamic works are normalized as $w^j_{\text{aero}} s/\bar{W}$ and $W^j_{\text{aero}}/\bar{W}$ with $\bar{W} = m\, s\, b^2\, (2\pi f_\alpha)^2\, \alpha_0$ [4].

Figure 5 (a) and (c) displays the spatial distribution of aerodynamic work $w^{j=2}_{\text{aero}} s/\bar{W}$ of the flutter mode (*i.e.* the 2nd aeroelastic mode) as a function of the reduced velocity U^* for Wing 1 and Wing 2, respectively. Positive values (red) correspond to destabilizing energy transfer from the airflow to the structure, while negative values (blue) indicate dissipative regions where energy is extracted from the structure to the airflow. Integrating the spanwise aerodynamic work over the span at each reduced velocity yields the total aerodynamic work acting on the structure, shown in Figure 5 (b) and (d) for Wing 1 and Wing 2, respectively. Flutter onset and offset are indicated by dotted lines. As discussed in subsection 4.3, the model predicts no instability for Wing 1 within the tested airspeed range. Note that structural damping is neglected in the aerodynamic work analysis, which allows a marginal instability to appear for Wing 1 over a narrow range of reduced velocity $3.1 < U^* < 3.9$.

Wing 1 is not prone to exchanging energy with the airflow. The aerodynamic work remains small in amplitude up to $U^* \simeq 4$, beyond which it decays sharply, a behaviour consistent with the hump-mode mechanism. The aerodynamic work density distribution reveals that this stabilisation originates from a large dissipative contribution localised near the wingtip (see Figure 5 (a)), resulting in a net negative aerodynamic work and a recovery of stability. In contrast, Wing 2 exhibits a strong stabilising aerodynamic work contribution at low reduced velocities, which decreases rapidly until flutter onset, reflecting a configuration more susceptible to energy exchange with the airflow and hence to flutter.

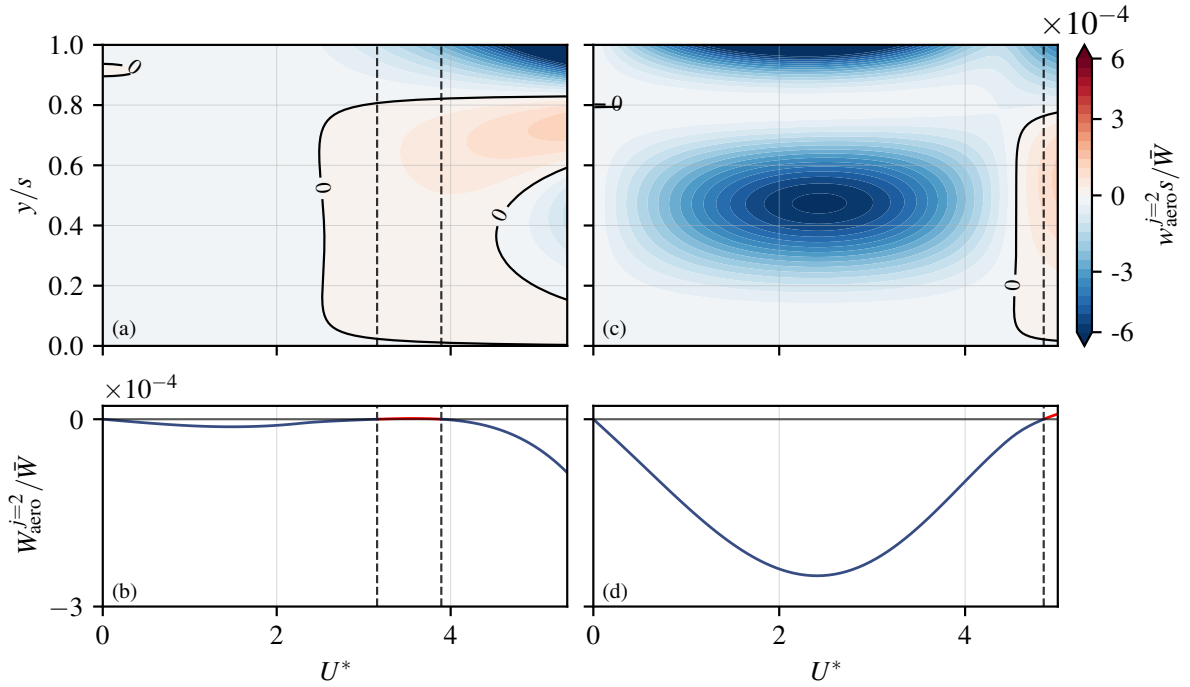

Figure 5: Spanwise distribution of dimensionless aerodynamic work $w^j_{\text{aero}}\, s/\bar{W}$ and total $W^j_{\text{aero}}/\bar{W}$ for the flutter mode ($j = 2$), for Wing 1 (a,b) and Wing 2 (c,d). Dotted lines indicate flutter onset and offset.

Recent studies have shown that accurate prediction of the critical flutter speed associated with B2-T1 coupling requires the inclusion of the B1 mode [3, 21]. Indeed, the B1 contribution plays a key role in the aerodynamic energy transfer mechanism and a stronger B1 participation

promotes a classical bending-torsion energy exchange, favouring flutter onset. To quantify this effect, the relative amplitude contributions of the bending modes are defined, for the j^{th} aeroelastic mode, as

$$\gamma_{h,i}^{j} = \frac{v_{h,i}^{j}}{b v_{\alpha,1}^{j}} \tag{8}$$

For both wings, the modulus and argument of $\gamma_{h,i}^{j=2}$ as a function of reduced velocity are shown in Figure 6. In both cases, the flutter mode is dominated by the second bending contribution ($i = 2$). For Wing 1, the B2 contribution reaches a minimum at $U^* \simeq 2.3$, where the spanwise aerodynamic work starts to become positive over approximately 75% of the span (see Figure 5(a)). However, the B2 contribution remains large compared to that of B1: over the instability range ($3.1 < U^* < 3.9$), $|\gamma_{h,2}^{j=2}/\gamma_{h,1}^{j=2}| \simeq 30$. In comparison, the B2 contribution of Wing 2 decreases monotonically with reduced velocity until reaching a plateau for $U^* > 4.5$. At $U^* \simeq 4.8$, where the total aerodynamic work becomes positive, $|\gamma_{h,2}^{j=2}/\gamma_{h,1}^{j=2}| \leq 3$ and the phase of B1 relative to T1 is positive, promoting a classical bending-torsion flutter mechanism.

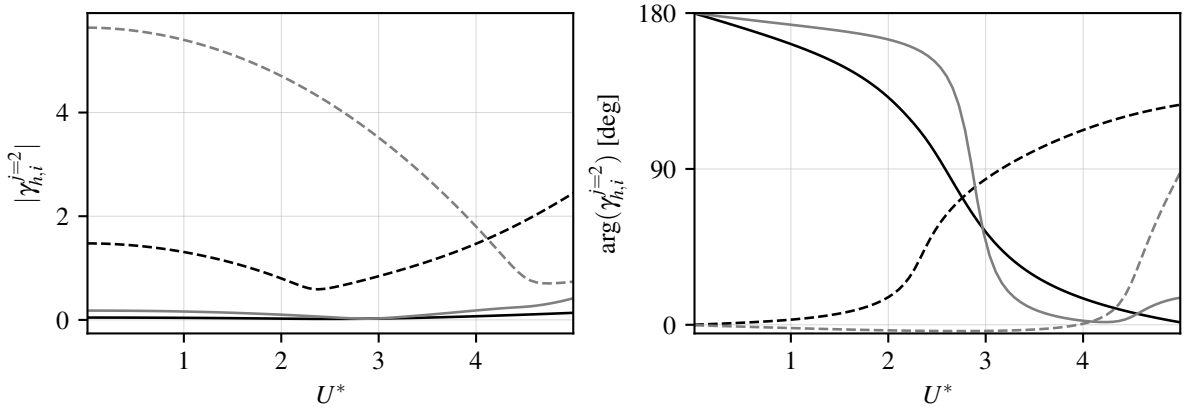

Figure 6: Dimensionless amplitude ratio $|\gamma_{h,i}^{j=2}|$ and associated phase angle $\arg(\gamma_{h,i}^{j=2})$ between the i^{th} bending mode and the 1^{st} torsional mode, for 1^{st} bending ($i = 1$): continuous line, 2^{nd} bending ($i = 2$): dashed line, as a function of reduced velocity, for Wing 1 (black) and Wing 2 (grey).

6 CONCLUSION

This study investigates the B2-T1 flutter mechanism in high-aspect-ratio wings by combining wind tunnel experiments on two taut-strip wings with a Rayleigh-Ritz/Theodorsen linear reduced-order model. Despite their geometric similarity, the two wings exhibit significantly different aeroelastic behaviours: Wing 1 remains stable while Wing 2 undergoes flutter, both displaying a hump-shaped damping variation.

The energy-based analysis shows that the B2 vibration mode produces alternating stabilising and destabilising regions along the span. The restabilisation observed in Wing 1 results from a strong dissipative contribution near the wingtip. The modal content analysis further shows that a larger B1 participation in Wing 2 enhances the bending-torsion energy exchange. These results confirm that the B2-T1 hump-mode instability is governed by the interplay between spanwise energy distribution, modal participation, and intermodal phase variation.

A STRUCTURAL AND AERODYNAMIC MATRICES

The structural matrices are given by

$$\mathbf{M}_S = \mathbf{M}_{S,\text{wing}} + \mathbf{M}_{S,\text{tip}}, \tag{9}$$

with

$$\mathbf{M}_{S,\text{wing}} = \begin{bmatrix} m\,\mathbf{\Phi}_{hh} & mX_\alpha\,\mathbf{\Phi}_{h\alpha} \\ mX_\alpha\,\mathbf{\Phi}_{\alpha h} & I_\alpha\,\mathbf{\Phi}_{\alpha\alpha} \end{bmatrix}, \quad \mathbf{M}_{S,\text{tip}} = \begin{bmatrix} M_\text{t}\,\mathbf{\Phi}_{hh} & M_\text{t}X_\text{t}\,\mathbf{\Phi}_{h\alpha} \\ M_\text{t}X_\text{t}\,\mathbf{\Phi}_{\alpha h} & I_{\text{t,y}}\,\mathbf{\Phi}_{\alpha\alpha} \end{bmatrix}_{y=s}, \tag{10}$$

where the subscript $y = s$ indicates that all mode shape products in $\mathbf{M}_{S,\text{tip}}$ are evaluated at the wing tip. The stiffness and damping matrices are

$$\mathbf{K}_S = \begin{bmatrix} EI_x\,\mathbf{\Phi}''_{hh} & \mathbf{0} \\ \mathbf{0} & GJ\,\mathbf{\Phi}'_{\alpha\alpha} \end{bmatrix}, \qquad \mathbf{C}_S = \begin{bmatrix} 2\zeta_h\,\mathbf{I}_{N_h} & \mathbf{0} \\ \mathbf{0} & 2\zeta_\alpha\,\mathbf{I}_{N_\alpha} \end{bmatrix} \sqrt{\text{diag}(\mathbf{K}_S)\ \text{diag}(\mathbf{M}_S)}. \tag{11}$$

where the modal submatrices are defined by

$$[\mathbf{\Phi}_{xy}]_{ij} = \int_0^s \phi_{x,i}\,\phi_{y,j}\,\mathrm{d}y, \quad \left[\mathbf{\Phi}'_{xy}\right]_{ij} = \int_0^s \phi'_{x,i}\,\phi'_{y,j}\,\mathrm{d}y, \quad \left[\mathbf{\Phi}''_{xy}\right]_{ij} = \int_0^s \phi''_{x,i}\,\phi''_{y,j}\,\mathrm{d}y, \tag{12}$$

for $1 \le i \le N_x$ and $1 \le j \le N_y$. The aerodynamic matrices follow the notation of [20]. Denoting the aerodynamic coefficient subscripts by the associated degree of freedom and its time-derivative order, these matrices read

$$\mathbf{M}_A = \rho b^2 \boldsymbol{\mathcal{A}}_{\ddot{q}}, \quad \mathbf{C}_A = \rho U b\,\boldsymbol{\mathcal{A}}_{\dot{q}}, \quad \mathbf{K}_A = \rho U^2 \boldsymbol{\mathcal{A}}_q, \tag{13}$$

where each matrix shares the common block structure

$$\boldsymbol{\mathcal{A}}_\bullet = \begin{bmatrix} L_{\bullet h}\,\mathbf{\Phi}_{hh} & L_{\bullet\alpha}\,b\,\mathbf{\Phi}_{h\alpha} \\ -M_{\bullet h}\,b\,\mathbf{\Phi}_{\alpha h} & -M_{\bullet\alpha}\,b^2\mathbf{\Phi}_{\alpha\alpha} \end{bmatrix}, \tag{14}$$

with $\bullet \in \{\ddot{\cdot}, \dot{\cdot}, \cdot\}$ corresponding to $\mathbf{M}_A$, $\mathbf{C}_A$, and $\mathbf{K}_A$, respectively. The aerodynamic coefficients are

$$\begin{aligned} L_{\ddot{h}} &= \pi, & L_{\ddot{\alpha}} &= -\pi a, \\ L_{\dot{h}} &= C_{L\alpha} F, & L_{\dot{\alpha}} &= C_{L\alpha}\left[F\left(\tfrac{1}{2} - a\right) + \tfrac{G}{k}\right] + \pi, \\ L_h &= -C_{L\alpha}\,kG, & L_\alpha &= C_{L\alpha}\left[F - kG\left(\tfrac{1}{2} - a\right)\right], \\ M_{\ddot{h}} &= \pi a, & M_{\ddot{\alpha}} &= -\pi\left(\tfrac{1}{8} + a^2\right), \\ M_{\dot{h}} &= 2\,C_{M\alpha} F, & M_{\dot{\alpha}} &= 2\,C_{M\alpha}\left[F\left(\tfrac{1}{2} - a\right) + \tfrac{G}{k}\right] - \pi\left(\tfrac{1}{2} - a\right), \\ M_h &= -2\,C_{M\alpha}\,kG, & M_\alpha &= 2\,C_{M\alpha}\left[F - kG\left(\tfrac{1}{2} - a\right)\right], \end{aligned} \tag{15}$$

where F and G are the real and imaginary parts of Theodorsen's function $C(k) = F + iG$, and $C_{L\alpha}$ and $C_{M\alpha}$ are the steady lift and moment slopes.

B MODAL PARAMETERS IDENTIFICATION

Figure 7 illustrates stabilisation diagrams resulting from the SSI-cov [16] procedure applied to Wing 1 at tested airspeeds. Tolerances are set to 1% for successive frequencies and 5% for damping ratios [17].

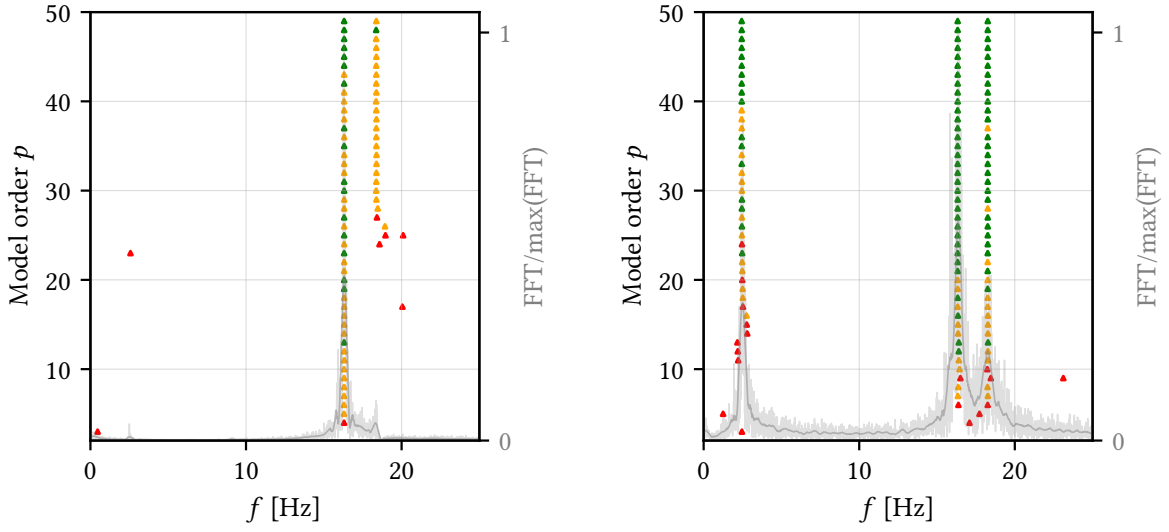

(a) $U = 0$ m/s

(b) $U = 10$ m/s

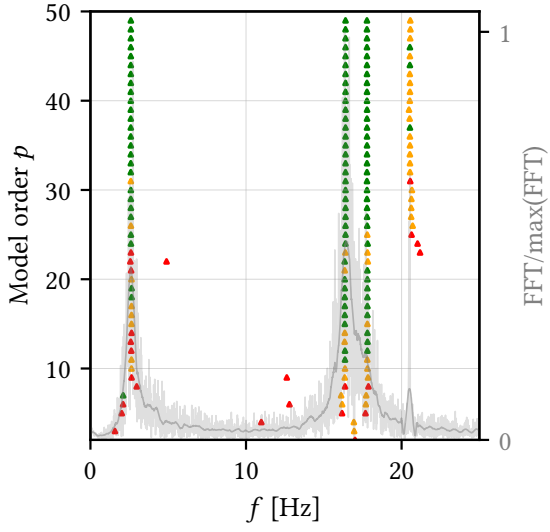

(c) $U = 20$ m/s

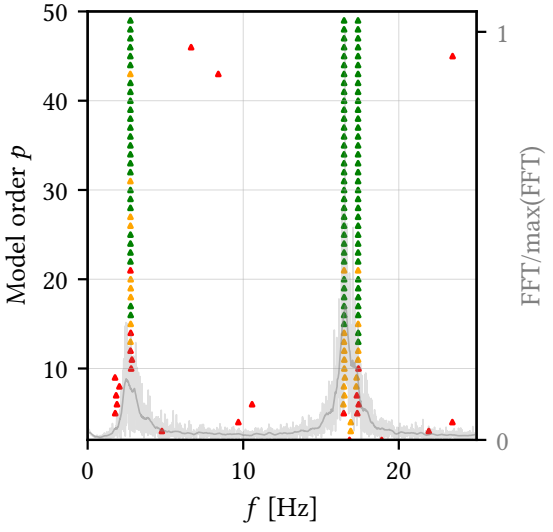

(d) $U = 25$ m/s

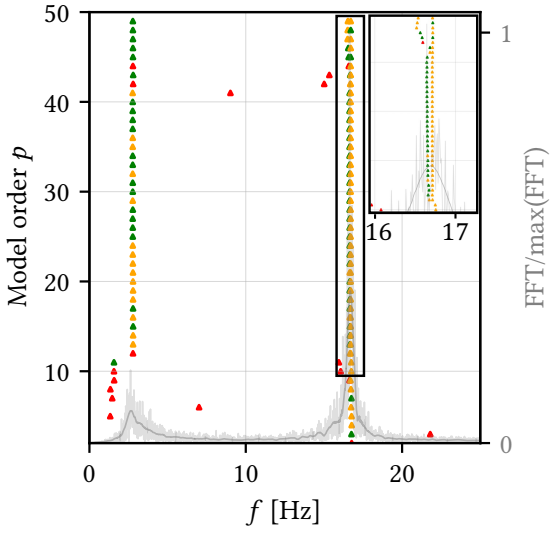

(e) $U = 30$ m/s

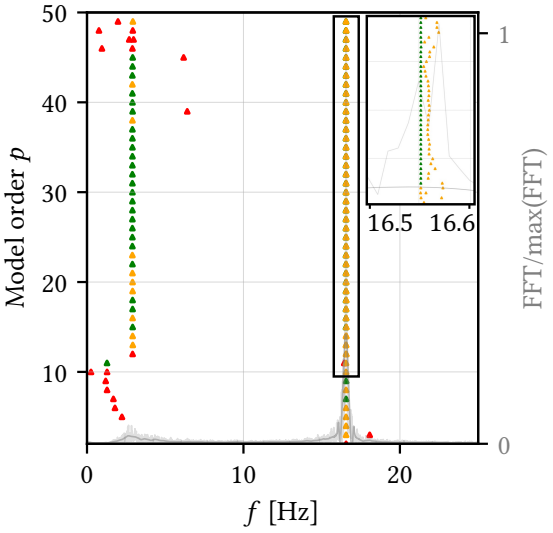

(f) $U = 33$ m/s

Figure 7: SSI-cov stabilisation diagrams for Wing 1 at selected airspeeds. Poles stable in frequency and damping (green), in frequency only (orange), and unstable (red). The normalised FFT is overlaid in grey.

C REFERENCES

[1] Afonso, F., Vale, J., Oliveira, E., et al. (2017). A review on non-linear aeroelasticity of high aspect-ratio wings. *Progress in Aerospace Sciences*, 89, 40–57. doi:10.1016/j.paerosci.2016.12.004.

[2] Bras, M., Warwick, S., and Suleman, A. (2022). Aeroelastic evaluation of a flexible high aspect ratio wing UAV: Numerical simulation and experimental flight validation. *Aerospace Science and Technology*, 122, 107400. doi:10.1016/j.ast.2022.107400.

[3] Vindigni, C. R., Mantegna, G., Orlando, C., et al. (2025). A refined aeroelastic beam finite element for the stability analysis of flexible subsonic wings. *Computers & Structures*, 307, 107618. doi:10.1016/j.compstruc.2024.107618.

[4] Bisplinghoff, R. L. and Ashley, H. (1962). *Principles of Aeroelasticity*. New York: Wiley & Sons.

[5] Dowell, E. H., Curtiss, H. C., Jr., Scanlan, R. H., et al. (1982). *A Modern Course in Aeroelasticity*. Sijthoff & Noordhoff.

[6] Berci, M. and Cavallaro, R. (2018). A hybrid reduced-order model for the aeroelastic analysis of flexible subsonic wings—a parametric assessment. *Aerospace*, 5(3), 76. doi:10.3390/aerospace5030076.

[7] Loring, S. (1944). Use of generalized coordinates in flutter analysis. Tech. Rep. 440156, SAE. doi:10.4271/440156.

[8] Tang, D. and Dowell, E. H. (2001). Experimental and theoretical study on aeroelastic response of high-aspect-ratio wings. *AIAA Journal*, 39(8), 1430–1441. doi:10.2514/2.1484.

[9] Ritter, M., Hilger, J., Ribeiro, A., et al. (2024). Collaborative Pazy wing analyses for the Third Aeroelastic Prediction Workshop. In *AIAA SCITECH 2024 Forum*. Orlando, FL: American Institute of Aeronautics and Astronautics. doi:10.2514/6.2024-0419.

[10] Stephan, C. and Amandolese, X. (2024). Design and experimental tests of a flexible wing of high aspect ratio for investigating flutter mechanisms. In *International Forum on Aeroelasticity and Structural Dynamics (IFASD)*. The Hague, Netherlands.

[11] Jonsson, E., Riso, C., Lupp, C. A., et al. (2019). Flutter and post-flutter constraints in aircraft design optimization. *Progress in Aerospace Sciences*, 109, 100537. doi:10.1016/j.paerosci.2019.04.001.

[12] Riso, C. and Cesnik, C. E. S. (2023). Geometrically nonlinear effects in wing aeroelastic dynamics at large deflections. *Journal of Fluids and Structures*, 120, 103897. doi:10.1016/j.jfluidstructs.2023.103897.

[13] Theodorsen, T. (1935). General theory of aerodynamic instability and the mechanism of flutter. Tech. Rep. Report No. 496, National Advisory Committee for Aeronautics (NACA).

[14] Prieur, B. (2023). Contrôle piézoélectrique des charges et instabilités aéroélastiques sur aile flexible. Research internship report, École Polytechnique, conducted at CNAM (LMSSC) under the supervision of X. Amandolese and B. Lossouarn.

[15] Pirnay, M. (2025). *Aeroelastic Analysis of a Slender Wing: Wind Tunnel Tests and Modelling*. Master's thesis, University of Liège, Liège, Belgium.

[16] Peeters, B. and De Roeck, G. (1999). Reference-based stochastic subspace identification for output-only modal analysis. *Mechanical Systems and Signal Processing*, 13(6), 855–878. doi:10.1006/mssp.1999.1249.

[17] Van der Auweraer, H. and Peeters, B. (2004). Discriminating physical poles from mathematical poles in high order systems: use and automation of the stabilization diagram. In *Proceedings of the 21st IEEE Instrumentation and Measurement Technology Conference*, vol. 3. pp. 2193–2198.

[18] Silva, E., Magluta, C., Roitman, N., et al. (2022). Development of a structural identification methodology with uncertainty quantification through the ssi and bootstrap techniques. *Mechanical Systems and Signal Processing*, 165, 108290. doi:10.1016/j.ymssp.2021.108290.

[19] Meirovitch, L. (2001). *Fundamentals of Vibrations*. Boston: McGraw-Hill.

[20] Wright, J. R. and Cooper, J. E. (2007). *Introduction to Aircraft Aeroelasticity and Loads*. Wiley.

[21] Berci, M. and Torrigiani, F. (2020). Multifidelity sensitivity study of subsonic wing flutter for hybrid approaches in aircraft multidisciplinary design and optimisation. *Aerospace*, 7(11), 161. doi:10.3390/aerospace7110161.

COPYRIGHT STATEMENT